

Learning Dynamics from Multicellular Graphs with Deep Neural Networks

Haiqian Yang,^{1,*} Florian Meyer,² Shaoxun Huang,¹ Liu Yang,³
Cristiana Lungu,² Monilola A. Olayioye,² Markus J. Buehler,^{1,4,5} and Ming Guo^{1,†}

¹*Department of Mechanical Engineering, Massachusetts Institute of Technology,
77 Massachusetts Ave., Cambridge, MA 02139, USA*

²*Institute of Cell Biology and Immunology, University of Stuttgart, Allmandring 31, 70569 Stuttgart, Germany*

³*Department of Computer Sciences, University of Wisconsin - Madison, Madison, WI 53706, USA*

⁴*Laboratory for Atomistic and Molecular Mechanics (LAMM),
Massachusetts Institute of Technology, 77 Massachusetts Ave., Cambridge, MA 02139, USA*

⁵*Center for Computational Science and Engineering,
Schwarzman College of Computing, Massachusetts Institute of Technology,
77 Massachusetts Ave., Cambridge, MA 02139, USA*

(Dated: July 9, 2024)

Multicellular self-assembly into functional structures is a dynamic process that is critical in the development and diseases, including embryo development, organ formation, tumor invasion, and others. Being able to infer collective cell migratory dynamics from their static configuration is valuable for both understanding and predicting these complex processes. However, the identification of structural features that can indicate multicellular motion has been difficult, and existing metrics largely rely on physical instincts. Here we show that using a graph neural network (GNN), the motion of multicellular collectives can be inferred from a static snapshot of cell positions, in both experimental and synthetic datasets.

I. INTRODUCTION

Collective cell movement is crucial during many biological processes, such as embryogenesis, vascularization, cancer metastasis, and wound healing [1–12]. The inference of cell motion from multicellular structures not only can provide valuable information for understanding these complex processes, but also have a broad impact on medical and engineering fields such as histology, organ-on-chip, and 3D bio-printing for drug screening and disease modeling [13]. Despite that modern optical microscopy has enabled visualizing the evolution of many living multicellular structures in real-time, the principles they follow to self-organize into a complex living structure is still a mystery [1, 13–15].

Over the past decade, collective cell movement has been primarily studied with non-equilibrium physics approaches [16, 17]. Particularly, recent theoretical and experimental studies have shown that cell collectives can undergo cell jamming and unjamming transitions, highlighting the relation between cell shapes and tissue fluidity [5, 8, 18–24]; a more ordered cell packing is more static, whereas a more disordered cell packing is associated with higher cell motility [Fig. 1(a)]. Nevertheless, these relations are categorical (i.e. jammed or unjammed), and it is still difficult to make continuous predictions of cell migratory dynamics [Fig. 1(b)]; for example, it was shown that cell shape is not sufficient to predict the average cell migration speed [25]. Given one

static snapshot of two fluid-like epithelial monolayers, at what resolution can we distinguish which one is more dynamic than the other? A continuous prediction of collective cell migratory dynamics can be potentially achieved by defining additional geometric order parameters to refine our definition of structural disorder, but it is unclear how to define a list of relevant parameters in a systematic way.

While classical mechanistic active-matter models rely on the assumptions of symmetries and constitutive relations, data-driven inference methods can potentially bypass some of these disadvantages [26–35]. Notably, recent developments in the graph-based deep neural networks (GNN) [36, 37] provide an opportunity to develop data-driven models of complex systems, especially focused on models that take advantage of known discrete structural features. For instance, some studies have used graph-based modeling to capture complex multiscale material phenomena including dynamic properties, in diverse systems ranging from glass-forming liquids, proteins, spatial transcriptomics, crystalline materials, to spider webs [38–43]. Other work has focused on dynamic material phenomena [44] using attention-based graph models in conjunction with denoising algorithms to model dynamic fracture. Besides, some recent studies have applied GNN to track microscopic motion including linking cell trajectories [45], and inferring rules that govern cell fate [46]. Nevertheless, to our knowledge, GNN models have not been applied to study the glassy dynamic behaviors of the mesoscale multicellular collectives; these multicellular systems are often represented with a vertex-model framework [19–22, 47] or network of cell-cell adjacencies [5, 12, 23, 48], making GNN models a suitable option to build data-driven algorithm to study their collective

* hqyang@mit.edu

† guom@mit.edu

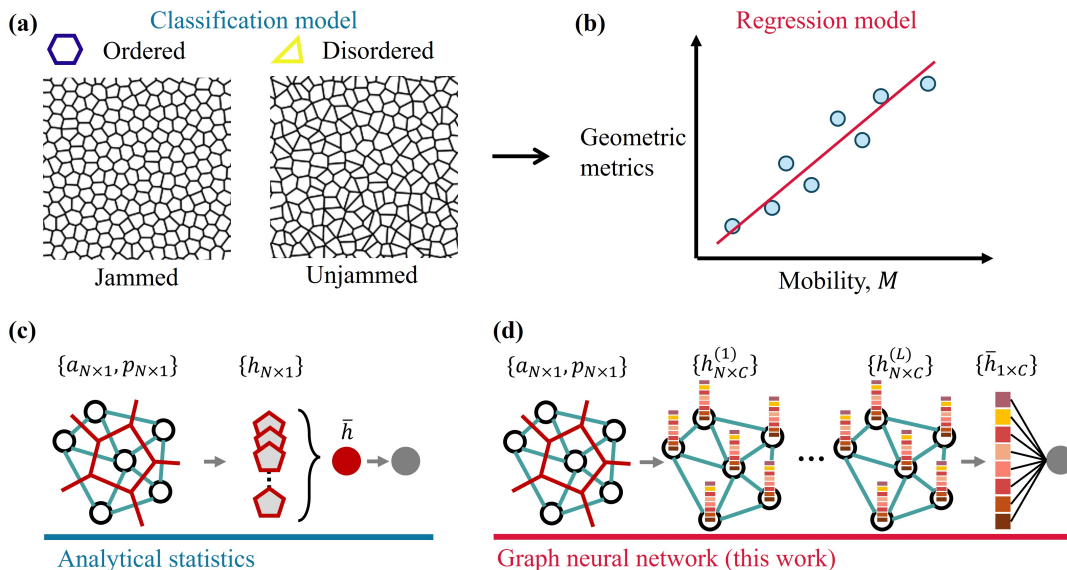


FIG. 1. Infer cell motion from static multicellular configurations using graph neural network (GNN). (a) Classification model. Typically an ordered configuration corresponds to a jammed state while a disordered configuration corresponds to an unjammed state [19, 21]. Cell boundaries are shown here. (b) It remains elusive what geometric feature of the static snapshot can be used to build a regression model to make continuous predictions of collective cell migratory dynamics. (c) A schematic configuration is shown on the left, with the coordinates of the cells represented by circles, and cell boundaries marked in red. An analytical model typically calculates a geometric feature for each cell $h_{N \times 1}$, from which an ensemble average \bar{h} is taken to reflect the structural disorder that correlates with collective cell dynamics. (d) Here, this geometric feature is replaced by a GNN with multiple graph convolutional layers and multiple hidden features $h_{N \times C}^{(l)}$ extracted from the training data through message-passing among neighboring cells via cell-cell adjacency \mathcal{E} , with $l \in \{1, 2, \dots, L\}$ the index of layers, and C the number of channels. Cyan, the cell-cell adjacency \mathcal{E} . The ensemble average $\bar{h}_{1 \times C}^{(L)}$ is then taken on the multi-channel hidden features of the last graph convolutional layer, from which the prediction is calculated using a final linear layer.

behaviors.

Here we propose to discover from static multicellular graph data the important spatial features that underlie collective cell migratory dynamics using GNN models [Fig. 1(d)]. The models are trained and validated on both experimental and synthetic datasets, achieving accurate predictions. Furthermore, a series of ablation studies indicate cell geometries and their spatial interactions are important features that help the model achieve accurate predictions.

II. PROBLEM SETUP

The system is given by a set of cell coordinates $\mathbf{r}_i(t) \in \mathbb{R}^{N \times d}$, where $\mathbf{r}_i(t)$ is the Cartesian coordinates of the i th cell in the frame t , and N is the total number of cells at frame t . We consider 2D systems ($d = 2$) in this study. The dimensionless cell coordinates can be defined as $\mathbf{r}_i^*(t) = a_c^{-1/2} \mathbf{r}_i(t)$, where a_c is a characteristic cell area (See Materials and Methods for details of a_c).

Mobility output.— We quantify the migratory dynamics by the dimensionless average traveled distance over a lag time τ , which we define as the mobility,

$$M(\tau) = \langle \Delta r^{*2}(\tau) \rangle^{\frac{1}{2}}, \quad (1)$$

where $\langle \Delta r^{*2}(\tau) \rangle$ is the dimensionless ensemble-averaged radial mean squared displacement. M is a measure of the average distance traveled relative to a characteristic cell size.

Graph input.— At time point $t = t_s$, from one snapshot of the dimensionless cell centroid coordinates $\mathbf{r}_i^*(t_s)$, Delaunay triangulation can be used to construct the cell-cell adjacency. Each input graph \mathcal{G} is given by [Fig. 1(d)]

$$\mathcal{G} = (\mathcal{N}, \mathcal{E}), \quad (2)$$

which contains cell centroids (nodes) $n_i \in \mathcal{N}$, $\mathcal{N} = \{1, 2, \dots, N\}$, and cell-cell adjacencies (undirectional Delaunay edges) $\mathbf{e}_k = (n_i, n_j) \in \mathcal{E}$, $\mathcal{E} \subseteq \mathbb{Z}^{2 \times E}$, with E the number of edges.

Each node is described by a feature vector $\mathbf{c}_i \in \mathbb{R}^{1 \times C}$, with C the dimension of input nodal features. Because the output M is invariant, we construct this input feature vector from invariant geometric quantities of the Voronoi tessellation. Two invariants, area and perimeter are shown to be particularly important in regulating tissue fluidity [19, 21]. Therefore, while higher order moments can be considered, here we consider $C = 2$ and

$$\mathbf{c}_i = (a_i, p_i) \quad (3)$$

with a_i the dimensionless area and p_i the dimensionless

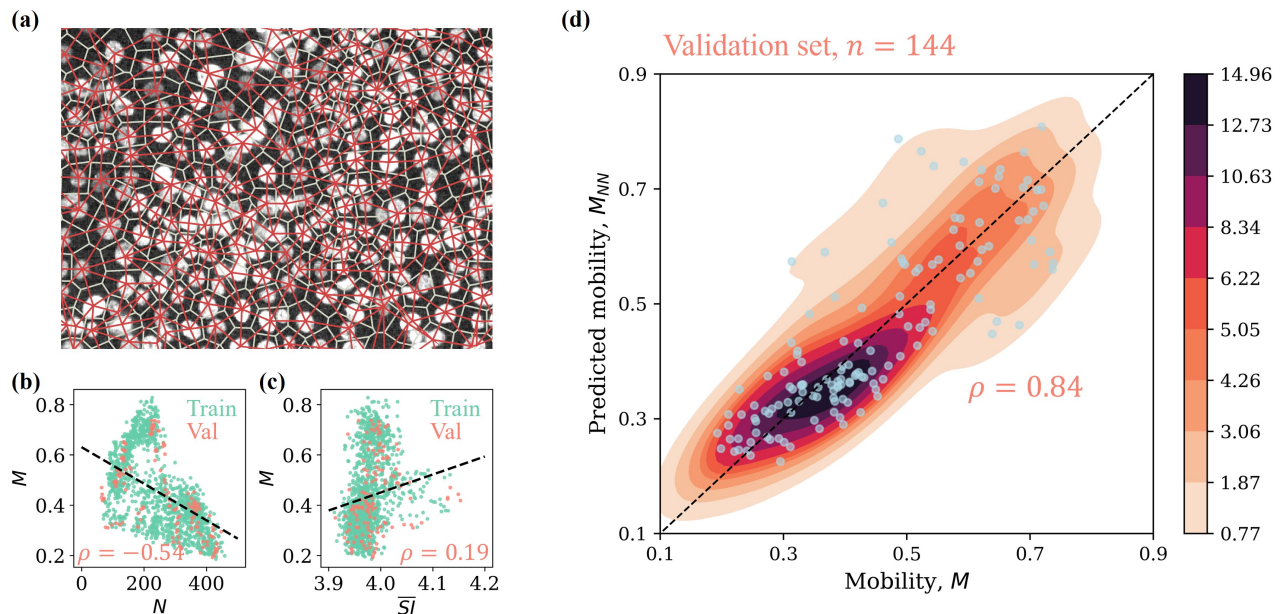


FIG. 2. Inferring cell motion $\tilde{M}(\mathbf{X}, \mathcal{G})$ from a snapshot in the experimental dataset of MCF-10A cell monolayers cultured on 2D substrates. (a) A zoom-in view of a representative snapshot of the dataset. Nuclei are stained for cell tracking. Green, Voronoi edges. Red, Delaunay edges. (b) Mobility M vs. cell number N in the region of interest (ROI) with the dimension $555.4 \mu\text{m} \times 401.1 \mu\text{m}$, calculated in the train set (green) and the validation set (orange). The black dashed line is a fitted linear function of M against N in the validation set. (c) Mobility M vs. median of cell shape index $\bar{S}I$ in the ROI, calculated in the train set (green) and the validation set (orange). The black dashed line is a fitted linear function of M against $\bar{S}I$ in the validation set. (d) Mobility prediction M_{NN} vs ground truth M in the validation set. The color map indicates probability density. The black dashed line is a reference line $M_{NN} = M$. In (b), (c), and (d), each dot indicates an individual snapshot (with $n = 1,296$ individual snapshots in the train set and $n = 144$ individual snapshots in the validation set). $\tau = 75$ minutes.

perimeter of the Voronoi cell of the node v_i . These feature vectors are organized in the feature matrix $\mathbf{X} = [\mathbf{c}_1 \mathbf{c}_2 \dots \mathbf{c}_N] \in \mathbb{R}^{N \times C}$.

Task.— The goal is to identify a neural network approximation of the following function

$$M(\tau) = \tilde{M}(\mathbf{X}, \mathcal{G}), \quad (4)$$

which relates a static snapshots of the system $(\mathbf{X}, \mathcal{G})$ at time point $t = t_s$ with the mobility $M(\tau)$.

III. RESULTS

A. Performance on experimental dataset

To test this approach in experimental multicellular systems, we first perform experiments to perturb cell motility and their static configurations. We use the non-tumorigenic human breast epithelial cell line MCF-10A as our model system. Previous studies have shown that epidermal growth factor (EGF) withdrawal can induce motility arrested phase [49], while transforming growth factor β (TGF β) treatment can enhance cell motility through an Epithelial-Mesenchymal-Transition (EMT)-like process [50, 51]. Besides the biochemical cues, biophysical environment such as cell density not only results

in glassy behaviors [18, 23], but also affects the formation of cell-cell junctions and contact inhibition mechanisms that maintain tissue homeostasis [52, 53]. Therefore, to generate a comprehensive dataset that covers a wide range of static structures and cell motility, we perform time-lapsed imaging of 2D MCF-10A monolayers under different conditions, including EGF withdrawal, TGF β treatment, and the control group with no treatment, each at a series of cell seeding densities (See [Supplemental Materials](#) for details of the experiments). We create an experimental dataset of 240 independent 16-hour time-lapsed videos of MCF-10A cell monolayers. Among the 240 videos, 196 videos are used to construct the training set, and 48 videos are used to construct the validation set. We select 6 well-separated frames of each video, each as one entry in the datasets, resulting in a total of 1,296 data entries for training, and 144 data entries for validation (see Materials and Methods for details regarding preparing the graph from raw videos).

The mobility M has a wide distribution ([Supplemental Materials](#) Fig. S2); on both train and validation sets, the apparent geometric metrics such as cell number N in the field of view or median cell shape index $\bar{S}I$ are only weakly correlated with the mobility M [Fig. 2(b) and (c)], with Pearson correlation of -0.54 and 0.19 respectively on the validation set, suggesting the need of additional

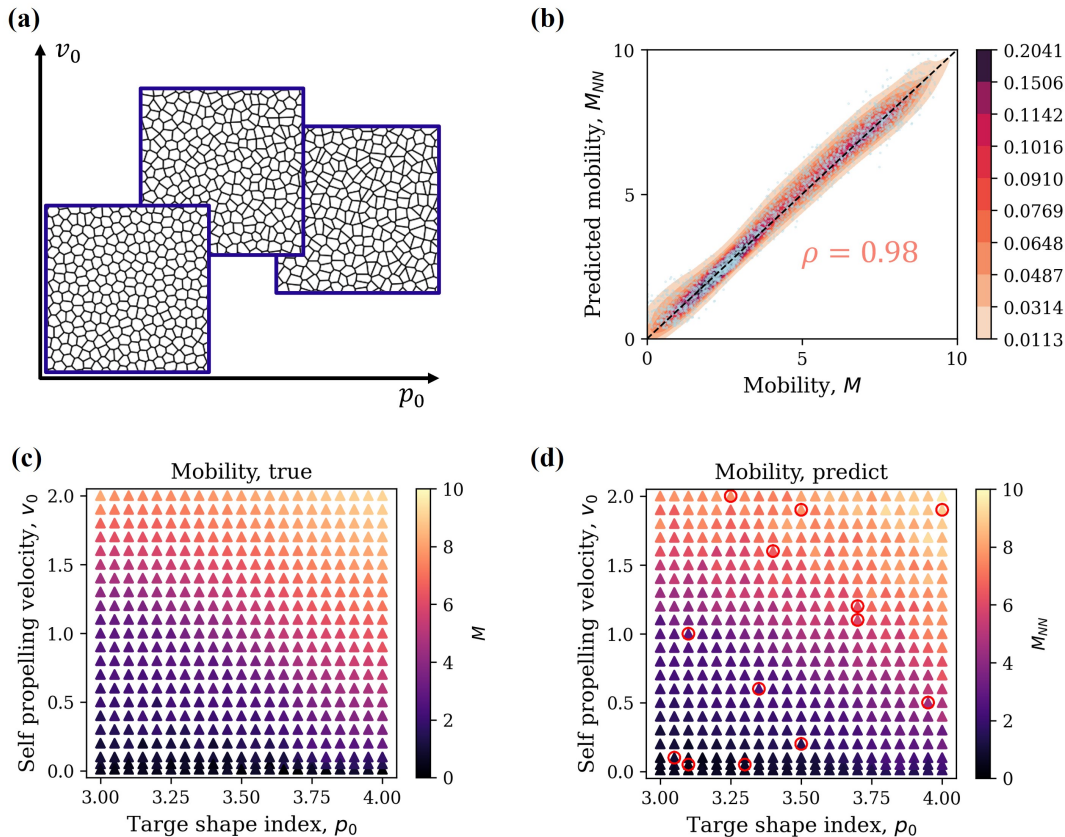


FIG. 3. The GNN model approximates $\tilde{M}(\mathbf{X}, \mathcal{G})$ in simulated cell monolayers. (a) Representative input graphs. (b) Prediction vs. ground truth. The color map indicates probability density, and each dot indicates an individual snapshot. The black dashed line is a reference line $M_{NN} = M$. (c) Ground-truth mobility landscape. The color map indicates the ground-truth mobility. (d) Predicted mobility landscape. Red markers, a small portion of the macroscopic state points ($N_s = 13$) are provided for training. The color map indicates the predicted mobility. $\tau = 20$.

structural features to further distinguish these systems.

Interestingly, the trained GNN model achieved highly accurate prediction of cell mobility M_{NN} from a snapshot of the system, with a Pearson correlation $\rho \sim 0.84$ between the prediction and ground truth [Fig. 2(d)]. Furthermore, we train the model on cell mobility at different lag times τ , and we find the trained models generate consistently accurate predictions across a range of τ from 30 minutes to 2 hours (Supplemental Materials Fig. S3 and Fig. S4).

B. Performance on synthetic dataset

To further test the GNN model, we use a synthetic dataset with continuously varying cell-cell interaction and self-propelling velocity at a constant cell number density. To do so, we use a dataset of simulated cell monolayers, containing steady-state 2D cell positions [21, 23]. Each simulation in the dataset is performed with different target shape index p_0 and self-propelling velocity v_0 , and the dataset consists of 462

distinct sets of configurations with different (p_0, v_0) [Fig. 3(c)]. The model is trained on a small number of state points, and is validated on the whole dataset. In this case, the GNN model can be considered as a universal function approximator to interpolate the mobility from the graphs without information about p_0 and v_0 . We observe that, with 4 state points provided, the GNN model can already achieve a Pearson correlation ρ of 0.9407 ± 0.0081 , while 9 state points for training can increase ρ to 0.9861 ± 0.0013 , and 36 state points are sufficient to increase ρ to 0.9932 ± 0.0007 (Supplemental Materials Table. S3). Here, from only 13 randomly selected state points, the GNN model achieves high accuracy with a Pearson correlation $\rho = 0.9867 \pm 0.0025$ and recovers the mobility landscape [Figs. 3(c&d)]. Furthermore, we train and validate models at various time scales τ , and we find that the models generate accurate predictions, with the performance increasing slightly at larger τ (Supplemental Materials Fig. S5 and Fig. S6).

To summarize, the predictions achieved by our GNN model indicate that static multicellular configurations contain critical features that can be utilized to predict

multicellular dynamics. While it has been challenging for classical mechanistic models to regress from static graphs toward dynamics, graph-based deep neural networks provide an alternative solution.

C. Ablation study

Features		Type of information		
Node	Edge	Geometric info.	Neighbor info.	Invariant
(a, p)	e	✓	✓	✓
(a, p)	-	✓		✓
-	e		✓	✓
(x, y)	e	✓	✓	

TABLE I. Four typical inputs are compared, with different combinations of information provided.

Intuitively, the GNN model achieves good performance with a minimal amount of data because it is capable of capturing nonlinear spatial interaction. To understand what information is indeed important for its performance, we further perform a series of training tasks with partial input information ablated or altered in both the training set and the validation set (Table I, Fig. 4).

By default, we provide area and perimeter (a, p) as node features together with cell-cell adjacency **e**; this achieves a Pearson correlation of $\rho = 0.8227 \pm 0.0242$ in the experimental dataset [Fig. 4(a)], and $\rho = 0.9867 \pm 0.0025$ in the synthetic dataset [Fig. 4(b)], both are significantly better than the baseline value which is 0.1939 in the experimental dataset and 0.7976 in the synthetic dataset.

Removing edges reduces ρ to 0.7636 ± 0.0216 in the experimental dataset and 0.9675 ± 0.0060 in the synthetic dataset. This highlights the importance of not only considering the geometry of each cell but also how the geometry differs in the local neighborhood of each cell. This agrees with recent studies showing cell neighborhood information such as cell-cell tension affects collective cell migratory dynamics both in simulations and in experiments [54, 55]; in the vertex-model framework, the cell-cell tension depends on the relative difference in the perimeter of two neighboring cells [24], which constitutes the simplest mechanism depending not only on single-cell geometry but also on the local neighborhood. On the other hand, fully removing the node feature decreases ρ to 0.4674 ± 0.0316 in the experimental dataset, and 0.8319 ± 0.0143 in the synthetic dataset. This is consistent with mechanistic theories showing cell shape is closely related to tissue fluidity [21]. Interestingly, adding cell positions (x, y) back instead as the node feature can only partially rescue the performance, with ρ to 0.6412 ± 0.0470 in the experimental dataset, and 0.8720 ± 0.0094 in the synthetic dataset. This implies

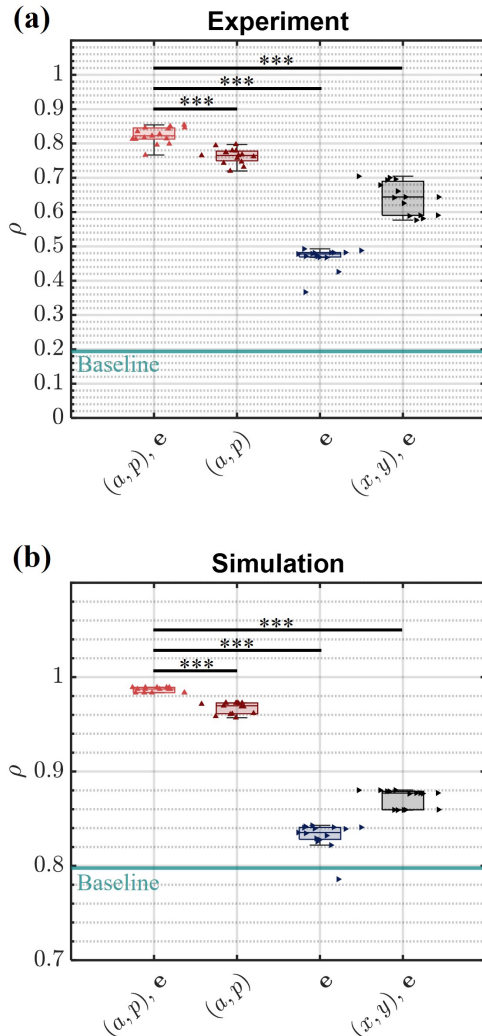


FIG. 4. Comparing the performance with different inputs on (a) the experiment dataset, and (b) the synthetic dataset. With each group, 3 independent models initialized with different random seed numbers are trained, and we report the performance on the validation set of the last 5 epochs. One-way ANOVA tests are performed to determine statistical significance. ***: p-value < 0.001. The baseline is the Pearson correlation between the mobility M and the median of the cell shape index \overline{SI} . Details of providing the ablated information are provided in the Materials and methods.

the benefits of considering symmetries when providing inputs to the model.

This ablation experiment suggests that cell geometries and their spatial interactions contain important features that can be used for accurate inference of tissue-level cell mobility. While classical mechanistic models heavily rely on intuitions and assumptions to distill a handful of structural metrics, graph-based deep neural networks are capable of bypassing these assumptions and discovering hidden relations from information about the whole graph.

IV. DISCUSSIONS

Here we apply a graph neural network (GNN) to approximate the relation between multicellular static structures and collective cell dynamics. Our results suggest that the static structures of cell monolayers contain sufficient information to infer cell migratory dynamics with reasonable accuracy; using ablation studies, we demonstrate the relative importance of different input features for the model performance. We present that GNN is a promising tool that can approximate relations between multicellular graph data and collective cell migratory dynamics that are otherwise difficult to express using analytical formulas with predetermined structural order parameters.

Besides cellular geometries, recent studies have shown that collective cell dynamics are also regulated by cellular biochemical identities such as actomyosin activities [54], tension remodeling [55], and the extracellular-signal-regulated kinase (ERK) pathway [56], and other studies have shown the role of nematic order [57]. GNN models could allow studying their interactions together with cell geometries by further concatenating these cellular identities as additional dimensions of the input features. Moreover, in several recent studies, inference of dynamic equations has been achieved on single-cell trajectories [29–31, 58]. It will be interesting to combine GNN with these inference methods for dense active matter and living tissues such as epithelia.

We envision that geometric deep-learning algorithms will provide a suitable tool for studying diverse physical phenomena in mesoscale multicellular living systems and dense active matter. We further discuss some of the possibilities in the [Supplemental Materials](#).

V. MATERIALS AND METHODS

Experimental dataset.— Experimental and data pre-processing details can be found in the [Supplemental Materials](#). Briefly, we use the non-tumorigenic human breast epithelial cell line MCF-10A to create the experimental dataset. The cells are cultured in a glass bottom 96-well plate (Greiner, No. 655891) coated with collagen R (Serva, No. 47254.01), and the nuclei are stained (SPY650-DNA) for cell tracking. The cells are imaged using WiScan Hermes High Content Imaging System (Idea Biomedical) every 3 minutes for 16 hours. To perturb both cell mobility and their static configuration, three types of treatment conditions (EGF withdrawal, TGF β treatment, and control) and 4 initial cell seeding number densities are used, and 20 independent locations of each condition are imaged, resulting in a total of 240 independent time-lapsed videos, covering a broad range of monolayer structures and cell mobility. Among the 240 videos, 196 videos are used to create the train set, and 48 videos are used to create the validation set.

Cell tracking is performed with a customized MAT-

LAB script adapted from the particle tracking algorithm [59]. Multiple frames at 1-hour intervals are selected from each video, resulting in a train set of 1,296 graphs, and a validation set of 144 graphs. The FOV of the raw videos has a dimension of $802\ \mu\text{m} \times 599\ \mu\text{m}$. The characteristic length scale $a_c^{1/2}$ is calculated as the $a_c^{1/2} = \sqrt{\frac{A_{FOV}}{\langle N \rangle}} = 30.9\ \mu\text{m}$ for our dataset, with A_{FOV} the area of the field of view (FOV), and $\langle N \rangle$ the average cell number across the full dataset consisting of 1440 graphs. For the input graphs \mathcal{G} , we filter out the distorted tiles at the boundary of the FOV, and the final region of interest (ROI) has a dimension of $555.4\ \mu\text{m} \times 401.1\ \mu\text{m}$.

Synthetic dataset.— The simulation dataset was created with Self-Propelled Voronoi simulations as previously described in [21, 23]. The dataset contains steady-state cell coordinates at 462 distinct state points at different (p_0, v_0) as shown in Fig. 3(c). Unless otherwise noted, we provide 7 distinct snapshots per state point to construct the full dataset ($n = 3, 234$), and we provide 13 randomly selected state points as marked in Fig. 3(d) for training ($n = 91$). Model performance with a different number of snapshots per state point or different state points provided for training is provided in the [Supplemental Materials](#).

Training GNN.— Details of the GNN model architecture are provided in the [Supplemental Materials](#). The Principal Neighbourhood Aggregation (PNA) graph convolutional layer is employed [36], and the models are implemented with PyTorch Geometric [60]. The mean squared error loss function is used throughout the paper.

Pearson correlation.— Throughout this study, the Pearson correlation factor ρ is used to evaluate and compare the performance of the models. The Pearson correlation factor ρ between the ground truth and prediction is calculated as

$$\rho = \frac{\sum(M_{NN} - \langle M_{NN} \rangle)(M - \langle M \rangle)}{\sqrt{\sum(M_{NN} - \langle M_{NN} \rangle)^2 \sum(M - \langle M \rangle)^2}}, \quad (5)$$

where the summation is taken over the whole validation set. $\langle M_{NN} \rangle$ and $\langle M \rangle$ denote average neural-network prediction and average ground truth respectively.

Ablation study.— To ablate the node feature, we replace the node feature matrix \mathbf{X} with 0. To ablate the edges, we replace the edge list \mathcal{E} with only self-loops (c_i, c_i) .

Baseline model.— Previous theoretical and experimental studies have identified the median of cell shape index \overline{SI} as a shape order parameter that defines the jamming-unjamming phase boundary of epithelia [19, 20]. The baseline performance is determined by the Pearson correlation between the median of the cell shape index \overline{SI} and the cell mobility M .

Statistics.— Performance is reported as mean \pm standard deviation. Statistic significance is determined using one-way ANOVA tests.

DATA AVAILABILITY

Our codes are available at
[https://github.com/GuoLab-CellMechanics/
 GNN-collective-cell-dynamics](https://github.com/GuoLab-CellMechanics/GNN-collective-cell-dynamics)

The experimental dataset will be made publicly available upon publishing this paper.

AUTHOR CONTRIBUTION

H.Y., M.B., and M.G. conceptualized this study. H.Y. performed this study. H.Y., L.Y., and M.B. wrote the machine learning algorithm. F.M., C.L., and M.A.O. collected the experimental cell monolayer data, and H.Y. and S.H. performed cell tracking. H.Y., M.B., and M.G.

wrote the paper.

ACKNOWLEDGEMENTS

We thank Dapeng Bi for providing the simulation dataset. We thank Roger Kamm, Zhenze Yang, Brendan Unikewicz, and Audrey Parker for the helpful discussions. The authors gratefully acknowledge the Technology Platform “Cellular Analytics” of the Stuttgart Research Center Systems Biology. MG acknowledges support from NIH (1R01GM140108). MJB acknowledges support from NIH (5R01AR077793). CL and MAO acknowledge supports from the Baden-Wuerttemberg Ministry of Science, Research and Arts. CL, MG and MAO received support from a Massachusetts Institute of Technology International Science and Technology Initiatives–Germany seed fund.

-
- [1] P. J. Keller, Imaging morphogenesis: technological advances and biological insights, *Science* **340**, 1234168 (2013).
- [2] F. Xiong, W. Ma, T. W. Hiscock, K. R. Mosaliganti, A. R. Tentner, K. A. Brakke, N. Rannou, A. Gelas, L. Souhait, I. A. Swinburne, *et al.*, Interplay of cell shape and division orientation promotes robust morphogenesis of developing epithelia, *Cell* **159**, 415 (2014).
- [3] K. McDole, L. Guignard, F. Amat, A. Berger, G. Malandain, L. A. Royer, S. C. Turaga, K. Branson, and P. J. Keller, In toto imaging and reconstruction of post-implantation mouse development at the single-cell level, *Cell* **175**, 859 (2018).
- [4] K. E. Kasza, S. Supriyatno, and J. A. Zallen, Cellular defects resulting from disease-related myosin ii mutations in drosophila, *Proceedings of the National Academy of Sciences* **116**, 22205 (2019).
- [5] X. Wang, M. Merkel, L. B. Sutter, G. Erdemci-Tandogan, M. L. Manning, and K. E. Kasza, Anisotropy links cell shapes to tissue flow during convergent extension, *Proceedings of the National Academy of Sciences* **117**, 13541 (2020).
- [6] W. Tang, A. Das, A. F. Pegoraro, Y. L. Han, J. Huang, D. A. Roberts, H. Yang, J. J. Fredberg, D. N. Kotton, D. Bi, *et al.*, Collective curvature sensing and fluidity in three-dimensional multicellular systems, *Nature Physics* **18**, 1371 (2022).
- [7] Y. L. Han, A. F. Pegoraro, H. Li, K. Li, Y. Yuan, G. Xu, Z. Gu, J. Sun, Y. Hao, S. K. Gupta, *et al.*, Cell swelling, softening and invasion in a three-dimensional breast cancer model, *Nature physics* **16**, 101 (2020).
- [8] W. Kang, J. Ferruzzi, C.-P. Spatarelu, Y. L. Han, Y. Sharma, S. A. Koehler, J. A. Mitchel, A. Khan, J. P. Butler, D. Roblyer, *et al.*, A novel jamming phase diagram links tumor invasion to non-equilibrium phase separation, *Iscience* **24** (2021).
- [9] J. S. Jeon, S. Bersini, M. Gilardi, G. Dubini, J. L. Charest, M. Moretti, and R. D. Kamm, Human 3d vascularized organotypic microfluidic assays to study breast cancer cell extravasation, *Proceedings of the National Academy of Sciences* **112**, 214 (2015).
- [10] I. K. Zervantonakis, S. K. Hughes-Alford, J. L. Charest, J. S. Condeelis, F. B. Gertler, and R. D. Kamm, Three-dimensional microfluidic model for tumor cell intravasation and endothelial barrier function, *Proceedings of the National Academy of Sciences* **109**, 13515 (2012).
- [11] H. Xu, Y. Huo, Q. Zhou, L. A. Wang, P. Cai, B. Doss, C. Huang, and K. J. Hsia, Geometry-mediated bridging drives nonadhesive stripe wound healing, *Proceedings of the National Academy of Sciences* **120**, e2221040120 (2023).
- [12] D. J. Skinner, B. Song, H. Jeckel, E. Jelli, K. Drescher, and J. Dunkel, Topological metric detects hidden order in disordered media, *Physical Review Letters* **126**, 048101 (2021).
- [13] R. D. Kamm, R. Bashir, N. Arora, R. D. Dar, M. U. Gillette, L. G. Griffith, M. L. Kemp, K. Kinlaw, M. Levin, A. C. Martin, *et al.*, Perspective: The promise of multi-cellular engineered living systems, *APL bioengineering* **2** (2018).
- [14] X. Trepap and E. Sahai, Mesoscale physical principles of collective cell organization, *Nature Physics* **14**, 671 (2018).
- [15] E. Karsenti, Self-organization in cell biology: a brief history, *Nature reviews Molecular cell biology* **9**, 255 (2008).
- [16] X. Trepap, M. R. Wasserman, T. E. Angelini, E. Millet, D. A. Weitz, J. P. Butler, and J. J. Fredberg, Physical forces during collective cell migration, *Nature physics* **5**, 426 (2009).
- [17] M. R. Shaebani, A. Wysocki, R. G. Winkler, G. Gompfer, and H. Rieger, Computational models for active matter, *Nature Reviews Physics* **2**, 181 (2020).
- [18] T. E. Angelini, E. Hannezo, X. Trepap, M. Marquez, J. J. Fredberg, and D. A. Weitz, Glass-like dynamics of collective cell migration, *Proceedings of the National Academy of Sciences* **108**, 4714 (2011).
- [19] J.-A. Park, J. H. Kim, D. Bi, J. A. Mitchel, N. T. Qazvini, K. Tantisira, C. Y. Park, M. McGill, S.-H.

- Kim, B. Gweon, *et al.*, Unjamming and cell shape in the asthmatic airway epithelium, *Nature materials* **14**, 1040 (2015).
- [20] D. Bi, J. Lopez, J. M. Schwarz, and M. L. Manning, A density-independent rigidity transition in biological tissues, *Nature Physics* **11**, 1074 (2015).
- [21] D. Bi, X. Yang, M. C. Marchetti, and M. L. Manning, Motility-driven glass and jamming transitions in biological tissues, *Physical Review X* **6**, 021011 (2016).
- [22] L. Atia, D. Bi, Y. Sharma, J. A. Mitchel, B. Gweon, S. A. Koehler, S. J. DeCamp, B. Lan, J. H. Kim, R. Hirsch, *et al.*, Geometric constraints during epithelial jamming, *Nature physics* **14**, 613 (2018).
- [23] H. Yang, A. F. Pegoraro, Y. Han, W. Tang, R. Abeyaratne, D. Bi, and M. Guo, Configurational fingerprints of multicellular living systems, *Proceedings of the National Academy of Sciences* **118**, e2109168118 (2021).
- [24] J. Huang, J. O. Cochran, S. M. Fielding, M. C. Marchetti, and D. Bi, Shear-driven solidification and non-linear elasticity in epithelial tissues, *Physical Review Letters* **128**, 178001 (2022).
- [25] J. H. Kim, A. F. Pegoraro, A. Das, S. A. Koehler, S. A. Ujwary, B. Lan, J. A. Mitchel, L. Atia, S. He, K. Wang, *et al.*, Unjamming and collective migration in mcf10a breast cancer cell lines, *Biochemical and biophysical research communications* **521**, 706 (2020).
- [26] M. S. Schmitt, J. Colen, S. Sala, J. Devany, S. Seetharaman, A. Caillier, M. L. Gardel, P. W. Oakes, and V. Vitelli, Machine learning interpretable models of cell mechanics from protein images, *Cell* **187**, 481 (2024).
- [27] F. Cichos, K. Gustavsson, B. Mehlig, and G. Volpe, Machine learning for active matter, *Nature Machine Intelligence* **2**, 94 (2020).
- [28] D. Brückner and C. P. Broedersz, Learning dynamical models of single and collective cell migration: a review, *Reports on Progress in Physics* (2024).
- [29] D. B. Brückner, A. Fink, C. Schreiber, P. J. Röttgermann, J. O. Rädler, and C. P. Broedersz, Stochastic nonlinear dynamics of confined cell migration in two-state systems, *Nature Physics* **15**, 595 (2019).
- [30] N. Romeo, A. Hastewell, A. Mietke, and J. Dunkel, Learning developmental mode dynamics from single-cell trajectories, *Elife* **10**, e68679 (2021).
- [31] D. B. Brückner, N. Arlt, A. Fink, P. Ronceray, J. O. Rädler, and C. P. Broedersz, Learning the dynamics of cell–cell interactions in confined cell migration, *Proceedings of the National Academy of Sciences* **118**, e2016602118 (2021).
- [32] J. LaChance, K. Suh, J. Clausen, and D. J. Cohen, Learning the rules of collective cell migration using deep attention networks, *PLoS computational biology* **18**, e1009293 (2022).
- [33] R. Supekar, B. Song, A. Hastewell, G. P. Choi, A. Mietke, and J. Dunkel, Learning hydrodynamic equations for active matter from particle simulations and experiments, *Proceedings of the National Academy of Sciences* **120**, e2206994120 (2023).
- [34] D. Bhaskar, W. Y. Zhang, and I. Y. Wong, Topological data analysis of collective and individual epithelial cells using persistent homology of loops, *Soft matter* **17**, 4653 (2021).
- [35] A. Frishman and P. Ronceray, Learning force fields from stochastic trajectories, *Physical Review X* **10**, 021009 (2020).
- [36] G. Corso, L. Cavalleri, D. Beaini, P. Liò, and P. Veličković, Principal neighbourhood aggregation for graph nets, *Advances in Neural Information Processing Systems* **33**, 13260 (2020).
- [37] T. N. Kipf and M. Welling, Semi-supervised classification with graph convolutional networks, *arXiv preprint arXiv:1609.02907* (2016).
- [38] V. Bapst, T. Keck, A. Grabska-Barwińska, C. Donner, E. D. Cubuk, S. S. Schoenholz, A. Obika, A. W. Nelson, T. Back, D. Hassabis, *et al.*, Unveiling the predictive power of static structure in glassy systems, *Nature Physics* **16**, 448 (2020).
- [39] Z. Yang and M. J. Buehler, Linking atomic structural defects to mesoscale properties in crystalline solids using graph neural networks, *npj Computational Materials* **8**, 198 (2022).
- [40] K. Guo and M. J. Buehler, Rapid prediction of protein natural frequencies using graph neural networks, *Digital Discovery* **1**, 277 (2022).
- [41] R. Viñas, C. K. Joshi, D. Georgiev, P. Lin, B. Dumitrescu, E. R. Gamazon, and P. Liò, Hypergraph factorization for multi-tissue gene expression imputation, *Nature machine intelligence* **5**, 739 (2023).
- [42] Y. Hu, J. Rong, Y. Xu, R. Xie, J. Peng, L. Gao, and K. Tan, Unsupervised and supervised discovery of tissue cellular neighborhoods from cell phenotypes, *Nature Methods* **21**, 267 (2024).
- [43] W. Lu, N. A. Lee, and M. J. Buehler, Modeling and design of heterogeneous hierarchical bioinspired spider web structures using deep learning and additive manufacturing, *Proceedings of the National Academy of Sciences* **120**, e2305273120 (2023).
- [44] M. J. Buehler, Modeling atomistic dynamic fracture mechanisms using a progressive transformer diffusion model, *Journal of Applied Mechanics* **89**, 121009 (2022).
- [45] J. Pineda, B. Midtvedt, H. Bachimanchi, S. Noé, D. Midtvedt, G. Volpe, and C. Manzo, Geometric deep learning reveals the spatiotemporal features of microscopic motion, *Nature Machine Intelligence* **5**, 71 (2023).
- [46] T. Yamamoto, K. Cockburn, V. Greco, and K. Kawaguchi, Probing the rules of cell coordination in live tissues by interpretable machine learning based on graph neural networks, *PLOS Computational Biology* **18**, e1010477 (2022).
- [47] H. Honda, Description of cellular patterns by dirichlet domains: the two-dimensional case, *Journal of theoretical biology* **72**, 523 (1978).
- [48] D. J. Skinner, H. Jeckel, A. C. Martin, K. Drescher, and J. Dunkel, Topological packing statistics distinguish living and non-living matter, *arXiv preprint arXiv:2209.00703* (2022).
- [49] S. E. Leggett, Z. J. Neronha, D. Bhaskar, J. Y. Sim, T. M. Perdikari, and I. Y. Wong, Motility-limited aggregation of mammary epithelial cells into fractal-like clusters, *Proceedings of the National Academy of Sciences* **116**, 17298 (2019).
- [50] S. E. Seton-Rogers, Y. Lu, L. M. Hines, M. Koundinya, J. LaBaer, S. K. Muthuswamy, and J. S. Brugge, Cooperation of the erbb2 receptor and transforming growth factor β in induction of migration and invasion in mammary epithelial cells, *Proceedings of the National Academy of Sciences* **101**, 1257 (2004).
- [51] K. Hosseini, A. Taubenberger, C. Werner, and E. Fischer-Friedrich, Emt-induced cell-mechanical changes enhance

- mitotic rounding strength, *Advanced Science* **7**, 2001276 (2020).
- [52] L.-M. Brenner, F. Meyer, H. Yang, A. R. Köhler, P. Bashtrykov, M. Guo, A. Jeltsch, C. Lungu, and M. A. Olayioye, Repeat dna methylation is modulated by adherens junction signaling, *Communications Biology* **7**, 286 (2024).
- [53] D. Hanahan and R. A. Weinberg, Hallmarks of cancer: the next generation, *cell* **144**, 646 (2011).
- [54] R. M. Herrera-Perez, C. Cupo, C. Allan, A. B. Dagle, and K. E. Kasza, Tissue flows are tuned by actomyosin-dependent mechanics in developing embryos, *PRX life* **1**, 013004 (2023).
- [55] F. Pérez-Verdugo and S. Banerjee, Tension remodeling regulates topological transitions in epithelial tissues, *PRX Life* **1**, 023006 (2023).
- [56] N. Hino, L. Rossetti, A. Marín-Llauradó, K. Aoki, X. Trepát, M. Matsuda, and T. Hirashima, Erk-mediated mechanochemical waves direct collective cell polarization, *Developmental cell* **53**, 646 (2020).
- [57] J.-M. Armengol-Collado, L. N. Carenza, J. Eckert, D. Krommydas, and L. Giomi, Epithelia are multiscale active liquid crystals, *Nature Physics* **19**, 1773 (2023).
- [58] D. B. Brückner, P. Ronceray, and C. P. Broedersz, Inferring the dynamics of underdamped stochastic systems, *Physical review letters* **125**, 058103 (2020).
- [59] J. C. Crocker and D. G. Grier, Methods of digital video microscopy for colloidal studies, *Journal of colloid and interface science* **179**, 298 (1996).
- [60] M. Fey and J. E. Lenssen, Fast graph representation learning with pytorch geometric, *arXiv preprint arXiv:1903.02428* (2019).
- [61] I. Loshchilov and F. Hutter, Decoupled weight decay regularization, *arXiv preprint arXiv:1711.05101* (2017).
- [62] S. H. Rudy, S. L. Brunton, J. L. Proctor, and J. N. Kutz, Data-driven discovery of partial differential equations, *Science advances* **3**, e1602614 (2017).
- [63] S. L. Brunton, J. L. Proctor, and J. N. Kutz, Discovering governing equations from data by sparse identification of nonlinear dynamical systems, *Proceedings of the national academy of sciences* **113**, 3932 (2016).
- [64] G. E. Karniadakis, I. G. Kevrekidis, L. Lu, P. Perdikaris, S. Wang, and L. Yang, Physics-informed machine learning, *Nature Reviews Physics* **3**, 422 (2021).
- [65] A. Saraswathibhatla, J. Zhang, and J. Notbohm, Coordination of contractile tension and cell area changes in an epithelial cell monolayer, *Physical Review E* **105**, 024404 (2022).
- [66] X. Yang, D. Bi, M. Czajkowski, M. Merkel, M. L. Manning, and M. C. Marchetti, Correlating cell shape and cellular stress in motile confluent tissues, *Proceedings of the National Academy of Sciences* **114**, 12663 (2017).
- [67] A. Musaelian, S. Batzner, A. Johansson, L. Sun, C. J. Owen, M. Kornbluth, and B. Kozinsky, Learning local equivariant representations for large-scale atomistic dynamics, *Nature Communications* **14**, 579 (2023).
- [68] J. Jumper, R. Evans, A. Pritzel, T. Green, M. Figurnov, O. Ronneberger, K. Tunyasuvunakool, R. Bates, A. Žídek, A. Potapenko, *et al.*, Highly accurate protein structure prediction with alphafold, *Nature* **596**, 583 (2021).

SUPPLEMENTAL MATERIALS

1. Details of the graph neural network model

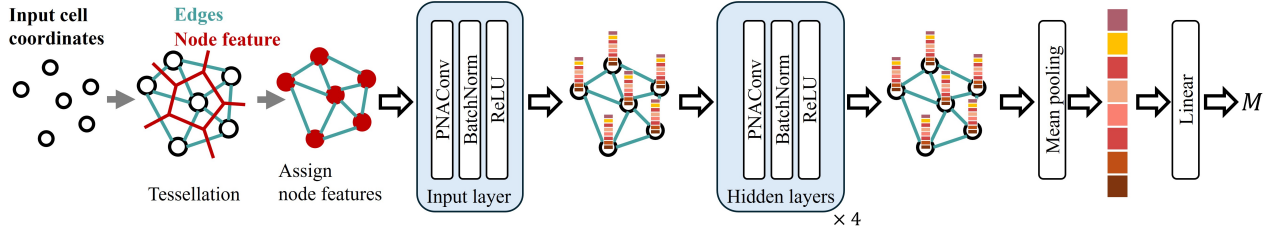


FIG. S1. Model architecture.

From cell coordinates, Voronoi tessellation is performed using `scipy.spatial.voronoi`, and the area a and perimeter p of the Voronoi cells are assigned as nodal features \mathbf{X} ; Delaunay tessellation is performed using `scipy.spatial.delaunay` to get the cell-cell adjacency as the graph edges \mathcal{E} . Unless otherwise specified, the network consists of 5 PNA convolutional layers [36] with 36 channels and 3 towers (model performance using different choices of hyperparameters is shown in Table. S1). ReLU activation function is used and batch norm layers are applied after each PNA layer. Global mean pooling and another linear layer are applied after the last PNA layer to transform to the output dimension (Fig. S1). In the PNA convolutional layers [36], we use `[sum, mean, std, max, min]` aggregators, along with `[identity, amplification, attenuation]` scalars. AdamW [61] with weight decay $1e-3$ is used. We use learning rate $1e-5$ for the experimental dataset and $1e-4$ for the synthetic dataset. All models are trained for 500 epochs. All models are trained and validated with an NVIDIA T4 GPU on Google Colab.

2. Additional discussions

a. Inference and generative tasks

While continuum hydrodynamic differential equations for physics systems, including active matter, are classically developed through symmetry argument and approximate free energy function with polynomial expansion, a significant effort has been made over the past decade to use neural networks for inferring the governing rules and equations from data [33, 62, 63], and to use physics-informed neural networks (PINN) to accelerate computation [64]. Similar opportunities exist in mesoscale dense active matter research, where the free energy function is usually assumed to be functions of certain invariant geometric quantities of cells (e.g. area and perimeter) in quadratic forms for simplicity. Designing a data-driven method to infer the forms and parameters of these terms in the governing equations from experimental data has remained a challenge. Doing so will be useful to refine the governing equations and free energy functions that have been widely used to simulate these mesoscale multicellular systems. For this task, compared to CNN which is more suitable for continuous fields, GNN is ideal for mesoscale active matter that has been widely described with Voronoi and Delaunay graphs for a long time [14, 21, 47].

Bridging discrete multicellular graphs and continuous fields, recent studies have also revealed an important correlation between multicellular structures and tissue stresses in epithelia in both experiments [65] and simulations [66]. In the context of generative deep learning algorithms, generating stress fields from graph data has been achieved using GNN on crystalline structures on synthetic datasets [39]. It is interesting to apply similar frameworks for inference of collective cell traction and tension fields from multicellular graphs. While invariance is enforced in the current study because the mobility measure M is an invariant quantity, in learning vector and tensor fields such as stresses, equivariant GNN structures [67] need to be considered.

b. Multi-body interactions in dense active matter

To further understand how graph-based learning might have gained additional insights into multicellular dynamics, we can consider a multi-body system whose dynamic equation is $\frac{d\mathbf{r}_i}{dt} = \mu\mathbf{F}(\{\mathbf{r}_i\}) + v_0\boldsymbol{\zeta}$, where \mathbf{r}_i is the Cartesian coordinates, t is time, \mathbf{F} is the interaction force that could in principle depend on all the degrees of freedom \mathbf{r}_i , $\boldsymbol{\zeta}$ is a unit noise term, μ is a coefficient and v_0 is the self-propelling velocity, $i = 1, 2, \dots, N$ is the index of the i th cell. While this is still an oversimplification of multicellular living systems, we can gain some insight into how learning might benefit from a graph-based construction.

Here the multi-body force $\mathbf{F}(\{\mathbf{r}_i\})$ is the unknown, and we are given a number of observations of $\{\mathbf{r}_i\}$. The task of either mechanistic models or deep learning models can be regarded as inferring either an analytical approximation or a neural network approximation for $\mathbf{F}(\{\mathbf{r}_i\})$, which is highly complex in living tissues. A straightforward choice is to expand $\mathbf{F}(\{\mathbf{r}_i\})$ as a sum of interaction terms [28]: $\mathbf{F}(\{\mathbf{r}_i\}) \simeq \sum_i \mathbf{F}^{(1)}(\mathbf{r}_i) + \sum_i \sum_j \mathbf{F}^{(2)}(\mathbf{r}_i, \mathbf{r}_j) + \sum_i \sum_j \sum_k \mathbf{F}^{(3)}(\mathbf{r}_i, \mathbf{r}_j, \mathbf{r}_k) + \dots$. In recent studies, several inference models have been constructed for active matter under this decomposition and a focus has been on estimating the two-body term $\sum_i \sum_j \mathbf{F}^{(2)}(\mathbf{r}_i, \mathbf{r}_j)$. The underlining assumption is that $|\mathbf{F}^{(n>2)}| \ll |\mathbf{F}^{(2)}|$. This assumption is generally true in classical systems, but in dense active matter such as living tissues, such interactions can be multi-body in nature, meaning that $|\mathbf{F}^{(n>2)}|$ is not necessarily negligible compared to $|\mathbf{F}^{(2)}|$, but rather depends on the relative cell-cell interactions across many cells. Graph-based learning provides an alternative option through estimating \mathbf{F} instead from the neighborhood of the cells represented as “graphs”. Notably, in more realistic situations where \mathbf{F} is not only a function of cell positions $\{\mathbf{r}_i\}$, but also a function of other multi-omics $\{\mathbf{o}_i\}$, GNN models are flexible enough to concatenate the information together as input embedding.

c. Efficient data representation, Multicellular Data Bank (MDB), and Large Multicellular Graph Model (LMGM)

Furthermore, we propose that a collaborative effort can be made to create a multicellular data bank (MDB) from which it will be possible to construct a large multicellular graph model (LMGM) for general-purposed predictions of the dynamic behaviors of multicellular living systems.

This century witnessed the fast growth of multicellular data for a variety of tissues and organs, yet it has been difficult to identify a universal model (either theoretical or computational) that can be predictive of the organization and dynamics of multicellular systems. Remarkably, it is still unclear what is a standard representation of multicellular data. Learning from data, the excellent performance of graph-based deep neural networks proves that multicellular graphs contain important hidden information that determines multicellular dynamics. On the other hand, from a

technical aspect, the raw multicellular data are high-dimensional, typically z-stacked (3D), time-lapse (dynamical), and multi-channel (multi-omics). The data size for a single biological sample at acceptable resolution can typically be on the order of 1-10 gigabytes. A large-scale deep neural network based on video representation greatly exceeds the current data process, transfer, and storage capacity. For the purpose of LMGM, it is required to have a standard efficient data representation that can condense the data while retaining the important information. The graph-based representation proposed in this study provides a possible solution. We note that while the nodal features and edges in the current analysis are purely geometrical, given the data we have at hand, important biological edges such as cell junctions and even long-ranged neurological connections can be further included in GNN models. Nevertheless, the positions of the cell nuclei can be used as the “backbone” of multicellular data, to which multi-omics data can be attached. While ideally dynamic multi-omic experiments can be performed in one round with multi-channel live staining, practically multiple experiments performed on one biological sample typically require multiple runs under multiple microscopes. Coordinate alignment can be first achieved using the coordinates of the cell nuclei. With the graph-based data representation and graph-based deep neural network, the pipeline proposed in this work, along with the accompanying implementations shared via open source code, provide a paradigm for systematically organizing multicellular data into a multicellular data bank, and further condensed into graph-based deep neural networks for general predictions.

At a smaller length scale, deep neural nets (e.g. AlphaFold) have successfully uncovered the folded structure of “graphs” of proteins [68]. In some recent studies, GNN models are shown to generate useful predictions within spatial transcriptomic datasets on fixed tissue samples [41, 42]. Nevertheless, it is still difficult to extend these data-driven efforts to dynamic time-lapsed video datasets of developmental processes consisting of a large number of cells evolving rapidly, with appropriate considerations of physical principles. We propose that it is possible to train a large model for general predictions of dynamic multicellular organization processes. The graph-based deep neural networks provide an excellent option that is capable of concatenating multi-omic biological inputs and outputs in an extremely flexible way. It will be interesting to further include genetics, proteomics, and other *in situ* multi-omic data as nodal features, and cell-cell junctions, mechanical interactions, and other interactions as edge features; these multi-omics graphs can then be provided to a graph neural network for prediction of missing or future features of these multicellular graphs evolving over time. Hence, we believe that the framework holds great potential for organizing fast-increasing multicellular data, and provides a possible solution to construct LMGM.

3. Data acquisition and pre-processing procedures

a. Experimental dataset

Cell culture and imaging procedures.— Non-tumorigenic human breast epithelial cell line MCF-10A is used to create the experimental dataset. Cells are cultured at 37 °C and 5% CO₂, with the full media of Dulbecco’s modified Eagle’s medium/F-12 supplemented with 5% horse serum, 20 ng ml⁻¹ epidermal growth factor (EGF), 0.5 μg ml⁻¹ hydrocortisone, 100 ng ml⁻¹ cholera toxin, 10 μg ml⁻¹ insulin, and 1% penicillin and streptomycin. 7 days before imaging, the parental cells are divided into two batches, with one batch still cultured in the full growth media, and the other batch cultured with the addition of 5 ng ml⁻¹ TGFβ1 (PeproTech, No. 100-21). 1 day before imaging, cells are seeded on collagen-coated glass-bottom 96-well plates in three groups. Group A is the parental cells cultured in full growth media, and it will be used as the control group during imaging. Group B is also the parental cells cultured in full growth media, and it will be starved of EGF during imaging (to be treated with growth media without EGF). Group C is the batch that has been treated with TGFβ1, and it is maintained with the same TGFβ1 treatment throughout the experiment. Each group is seeded at 4 cell number densities at 15,000, 20,000, 25,000, and 30,000 cells per well. Around 2 hours before imaging, the cells are washed 2 times with serum-free media. Then the full growth media is added to group A, growth media without EGF is added to group B, and full growth media supplemented with 5 ng ml⁻¹ TGFβ1 is added to group C, with all supplemented with SPY-650-DNA for cell tracking. 20 distinct locations of each condition are imaged simultaneously at 3 minutes per frame for 16 hours, with a field of view of 802 μm × 599 μm at 1382 × 1032 pixels. In total, this results in 240 videos (each with 320 frames) covering a wide range of cell mobility (Main text, Fig. 2).

Cell tracking.— Before tracking, the video resolutions are downsampled by 2, resulting in 691 × 516 pixels (resolution is 1.16 μm per pixel). The cells are tracked using a customized MATLAB script adapted from the particle tracking algorithm [59].

Frame selection.— We select the middle section of the videos for optimal video stability and tracking quality. Frames 100, 120, 140, 160, 180 and 200 from each video as one data entry to construct the whole dataset. The frames are sparsely selected to reduce the correlations among the graphs. This results in a total of $K = 1440$ graphs as inputs.

Normalization.— The characteristic area is calculated as $a_c = \frac{A_{FOV}}{\langle N \rangle}$, with the total area of the field of view $A_{FOV} = 691 \times 516 \text{ pixels}^2$ and $\langle N \rangle = \frac{1}{K} \sum_k^K N_k$ the average cell number per field of view, where $K = 1440$ is the total number of graphs in the full dataset. The length scale $a_c^{1/2} = 26.6 \text{ pixel}$ (30.9 μm) in this case.

The normalized cell coordinates are calculated as

$$\mathbf{r}_i^* = a_c^{-1/2} \mathbf{r}_i. \quad (6)$$

The field of view after normalization has a dimension of $x \in [0, 26.0]$ and $y \in [0, 19.4]$.

Calculating mobility.— Around each selected frame t_s , the mobility is defined as

$$M = \langle \Delta r^{*2}(\tau) \rangle^{\frac{1}{2}}, \quad (7)$$

where the dimensionless mean squared displacement $\langle \Delta r^{*2}(\tau) \rangle$ is calculated as

$$\langle \Delta r^{*2}(\tau) \rangle = \text{Var}(\mathbf{r}_i^*(t + \tau) - \mathbf{r}_i^*(t)) \Big|_{i,t}, \quad (8)$$

with $\text{Var}(\cdot) \Big|_{i,t}$ the variance taken both among cells and within the frame range $t \in [t_s - w, t_s + w]$, with $w = 60$ frames (3 hours).

Input graphs.— For each frame, Delaunay tessellation is first performed, generating a list of edges. Then Voronoi tessellation is performed. To clean the distorted cells and edges at the boundary of the field of view, we select a region of interest (ROI) $x \in [4, 22]$ and $y \in [3, 16]$, and only keep nodes that have all their associated vertices within the ROI.

Train and validation datasets.— The full dataset contains a total of 12 conditions from 3 treatment groups and 4 seeding densities each at 20 independent locations, among which we use locations 1-18 for the train set, and locations 19-20 for the validation set. The mobility distribution of the 3 treatment groups as a function of cell number N in the ROI and median shape index \overline{SI} of the full dataset consisting of $K = 1440$ graphs is shown in Fig. S2. All the graphs are treated equally and mixed in the datasets, and any information about the experimental condition is not provided to the GNN models.

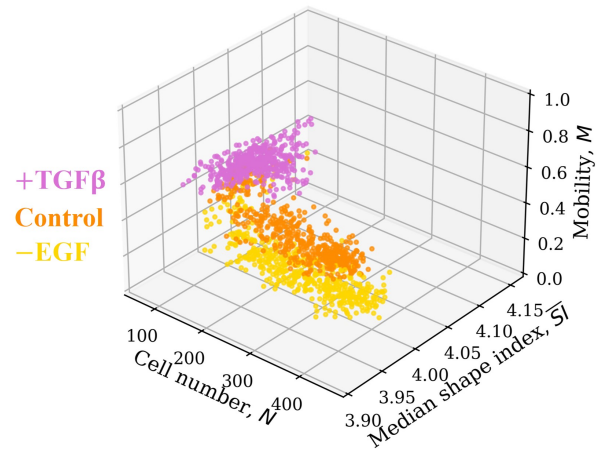


FIG. S2. The mobility M distribution of the full dataset with $K = 1440$ graphs. M at lag time $\tau = 75$ minutes is shown here. Each dot corresponds to a graph. Note that all the graphs are treated equally and mixed in the datasets, and any information about the experimental condition, including the treatment type information (+TGF β , Control, -EGF), is not provided to the model.

b. *Synthetic dataset*

Basic information.— The raw dataset contains Self-Propelled Voronoi (SPV) simulations at 462 distinct state points covering a broad range of cell target shape index and self-propelling velocity. Each simulation contains 4,000 frames of $N = 400$ cells within a simulation box of dimension $x \in [0, 20]$ and $y \in [0, 20]$, and therefore the characteristic length scale $a_c^{1/2} = 1$ in the simulation.

Frame selection.— Unless otherwise noted, we select 13 random state points for training as indicated in Fig. 3(d), and we select frame 500 to frame 3500 with a step size of 500, resulting in 7 frames per state point. The frames are sparsely selected to reduce the correlation among the graphs. Model performance of selecting a different number of frames per state points or selecting different state points for training are shown in Table. S2, Table. S3 and Fig. S7.

Calculating mobility.— The cell mobility M is calculated the same as in the experimental dataset with $w = 100$.

Input graphs.— The input graphs are constructed in the same way as in the experimental dataset. We select ROI as $x \in [2, 18]$ and $y \in [2, 18]$.

Output normalization for training.— The synthetic dataset covers a much broader range of cell mobility, with the maximal M on the order of 10 in a highly fluid-like system. For the benefit of using consistent hyperparameters in training the neural network, it is helpful to rescale the output around 1. Therefore, we rescale M as $\hat{M} = M/M_c$, with $M_c = 10$ when providing the data to the GNN model. That is, the direct output of the GNN is \hat{M} , and we scale \hat{M} back to its original range by $M_{NN} = M_c \hat{M}$ for all post-processing and visualization.

4. Additional results

a. Performance at different time scales

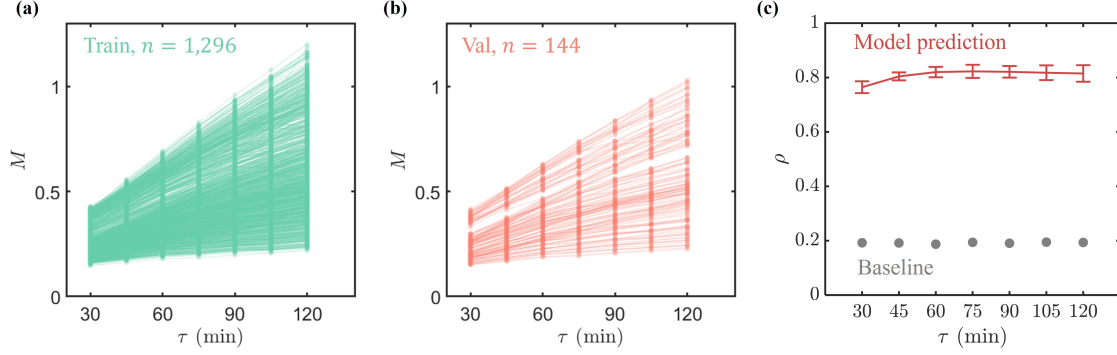


FIG. S3. Performance on the experimental dataset at different time scales. Mobility $M(\tau)$ at different time scales in the training set (a) and the validation set (b). (c) The GNN performance at different time scales. The error bar shows the standard deviation. The baseline is determined by the Pearson correlation between M and the median of cell shape index \overline{SI} at time scale τ .

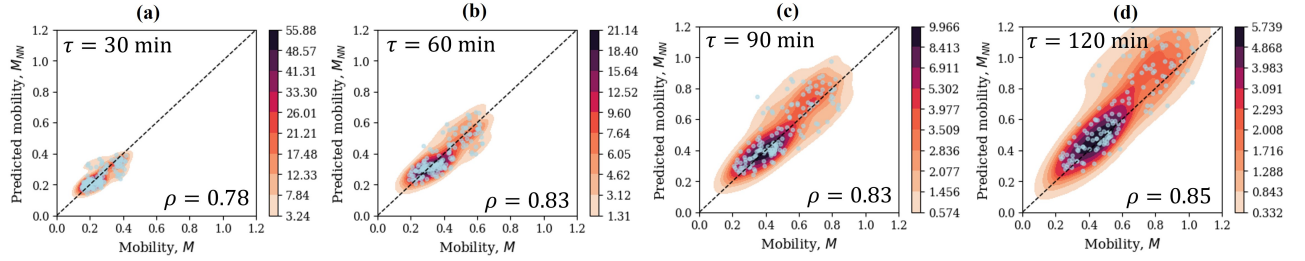


FIG. S4. GNN predictions vs. ground truth at different timescales on the experimental dataset. (a) $\tau = 30$ min. (b) $\tau = 60$ min. (c) $\tau = 90$ min. (d) $\tau = 120$ min.

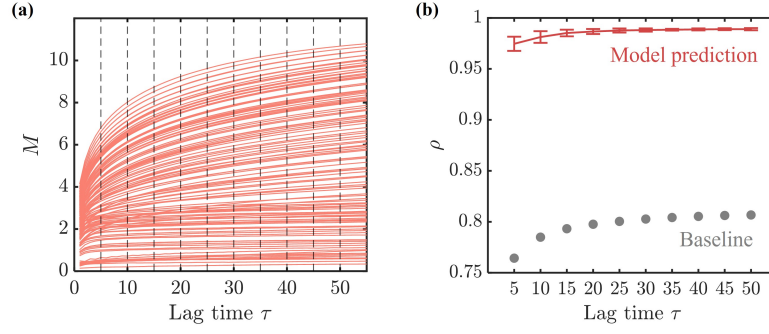


FIG. S5. Performance on the synthetic dataset at different time scales. (a) Mobility $M(\tau)$ at different time scales. Each line is an independent simulation, with $p_0 \in \{3.0, 3.1, 3.2, 3.3, 3.4, 3.5, 3.6, 3.7, 3.8, 3.9, 4.0\}$ and $v_0 \in \{0.01, 0.2, 0.4, 0.6, 0.8, 1.0, 1.2, 1.4, 1.6, 1.8, 2.0\}$. The dashed line marks the time scales that the GNN models are trained and validated. (b) The GNN performance. The error bar shows the standard deviation. The baseline is determined by the Pearson correlation between M and the median of cell shape index \overline{SI} at time scale τ .

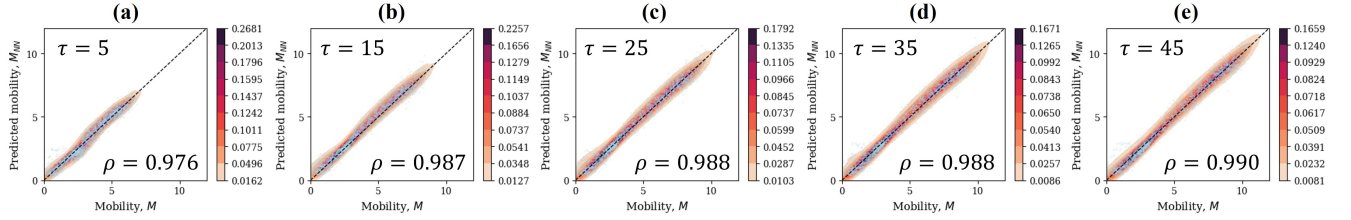


FIG. S6. GNN predictions vs. ground truth at different timescales on the synthetic dataset. (a) $\tau = 5$. (b) $\tau = 15$. (c) $\tau = 25$. (d) $\tau = 35$. (e) $\tau = 45$.

5. Effect of model hyperparameters

Layer	Channel	Batch size	Learning rate	ρ
5	36	128	1e-05	0.841 \pm 0.010
3	36	128	1e-05	0.828 \pm 0.005
4	36	128	1e-05	0.839 \pm 0.012
6	36	128	1e-05	0.771 \pm 0.012
7	36	128	1e-05	0.819 \pm 0.027
5	12	128	1e-05	0.796 \pm 0.003
5	24	128	1e-05	0.835 \pm 0.027
5	48	128	1e-05	0.808 \pm 0.028
5	60	128	1e-05	0.824 \pm 0.012
5	36	256	1e-05	0.840 \pm 0.007
5	36	32	1e-05	0.830 \pm 0.009
5	36	64	1e-05	0.820 \pm 0.023
5	36	128	1e-04	0.777 \pm 0.092
5	36	128	1e-06	0.807 \pm 0.001

TABLE S1. Effect of hyperparameters. On the experimental dataset, we train all models for 500 epochs and use random seed number 12345. The performance is reported as the mean \pm standard deviation of the last 5 epochs on the validation set.

6. Effect of dataset size

Number of frames per state points	ρ
2	0.9807 \pm 0.0068
7	0.9867 \pm 0.0025

TABLE S2. Performance of the model with different number of frames per state point provided in the training set. The raw dataset contains 4000 frames of steady-state configuration; here for the 2-frame group, the frames with frame index $\in \{500, 3500\}$ are provided each as one separate data entry in the train set, and for the 7-frame group, the frames with frame index $\in \{500, 1000, 1500, 2000, 2500, 3000, 3500\}$ are provided each as one separate data entry in the train set. For both, the 13 state points as shown in Fig. 3(d) are provided. For consistent comparison, all models are validated on the full dataset consisting of 462 state conditions each with 7 frames $\in \{500, 1000, 1500, 2000, 2500, 3000, 3500\}$.

State points	ρ
2 \times 2	0.9407 \pm 0.0081
3 \times 3	0.9861 \pm 0.0013
4 \times 4	0.9895 \pm 0.0009
5 \times 5	0.9880 \pm 0.0046
6 \times 6	0.9932 \pm 0.0007

TABLE S3. Performance of the models with different number of state points provided in the training set. The corresponding state points (p_0, v_0) provided in the training set are marked in Fig. S7.

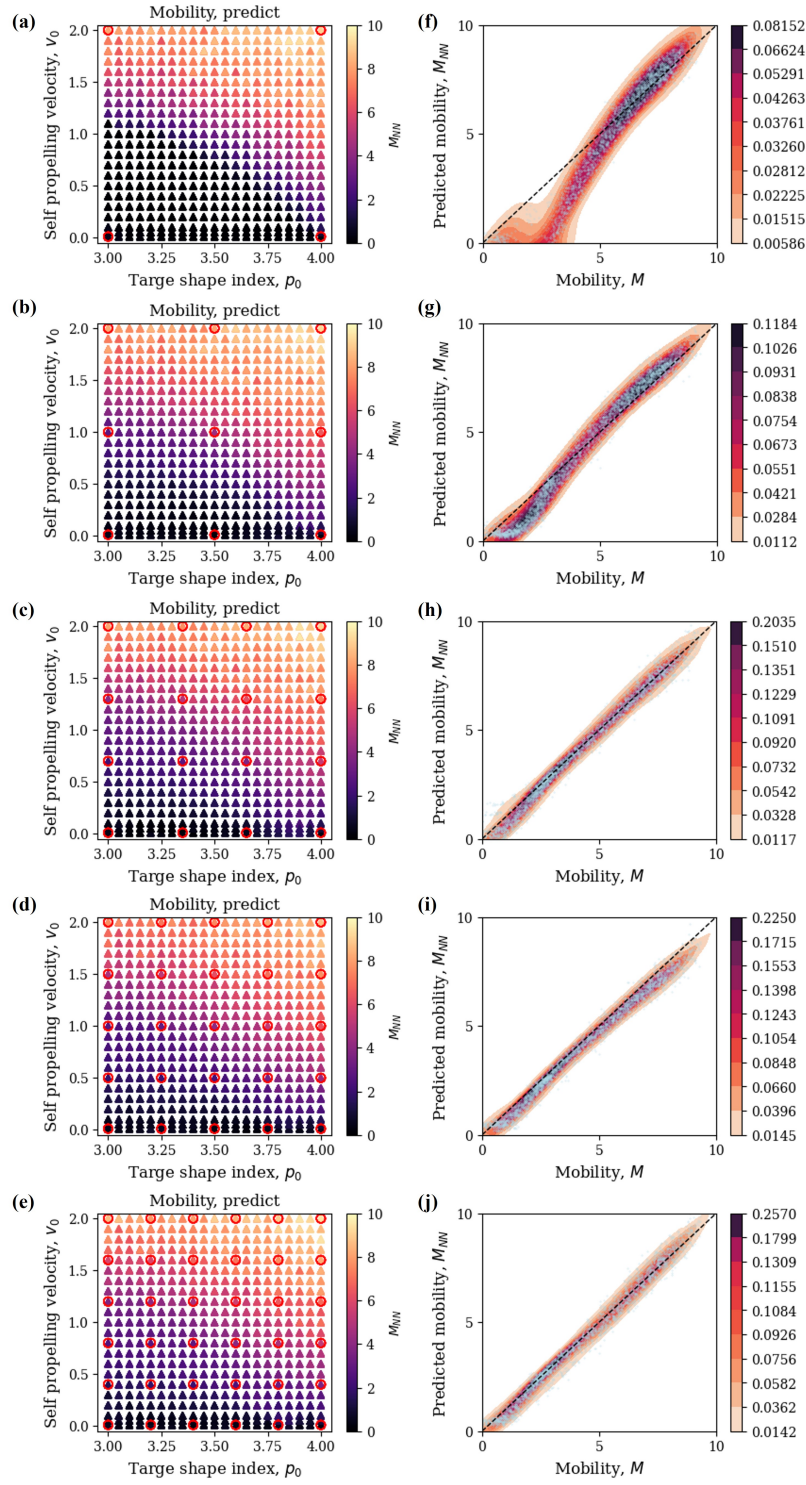


FIG. S7. The effect of states provided for training. (a-e) The predicted mobility landscape. The red markers indicate the states provided for training. (f-j) Prediction vs. ground truth. The color map indicates probability density and each scatter point represents one input graph.